

# Coherent spin-wave transport in an antiferromagnet

J.R. Hortensius<sup>1\*</sup>, D. Afanasiev<sup>1†</sup>, M. Matthiesen<sup>1</sup>, R. Leenders<sup>2</sup>, R. Citro<sup>3</sup>, A.V. Kimel<sup>4</sup>,  
R.V. Mikhaylovskiy<sup>2</sup>, B.A. Ivanov<sup>5</sup>, and A.D. Caviglia<sup>1§</sup>

<sup>1</sup>*Kavli Institute of Nanoscience, Delft University of Technology, P.O. Box 5046, 2600 GA Delft, The Netherlands.*

<sup>2</sup>*Department of Physics, Lancaster University, Bailrigg, Lancaster LA1 4YW, United Kingdom*

<sup>3</sup>*Dipartimento di Fisica “E.R. Caianiello”, Università di Salerno and Spin-CNR, I-84084 Fisciano (Sa), Italy*

<sup>4</sup>*Institute for Molecules and Materials, Radboud University Nijmegen, 6525 AJ Nijmegen, The Netherlands.*

<sup>5</sup>*Institute of Magnetism, National Academy of Sciences and Ministry of Education and Science, 03142 Kyiv, Ukraine.*

‡These authors contributed equally to this work

\* j.r.hortensius@tudelft.nl

† dmytro.afanasiev@physik.uni-regensburg.de

§ a.caviglia@tudelft.nl

**Magnonics is a research field complementary to spintronics, in which the quanta of spin waves (magnons) replace electrons as information carriers, promising less energy dissipation<sup>1-3</sup>. The development of ultrafast nanoscale magnonic logic circuits calls for new tools and materials to generate coherent spin waves with frequencies as high, and wavelengths as short, as possible<sup>4,5</sup>. Antiferromagnets can host spin waves at THz frequencies and are therefore seen as a future platform for the fastest and the least dissipative transfer of information<sup>6-11</sup>. However, the generation of short-wavelength coherent propagating magnons in antiferromagnets has so far remained elusive. Here we report the efficient emission and detection of a nanometer-scale wavepacket of coherent propagating magnons in antiferromagnetic DyFeO<sub>3</sub> using ultrashort pulses of light. The subwavelength confinement of the laser field due to large absorption creates a strongly non-uniform spin excitation profile, enabling the propagation of a broadband continuum of coherent THz spin waves. The wavepacket features magnons with detected wavelengths down to 125 nm that propagate with supersonic velocities of more than 13 km/s into the material. The long-sought source of coherent short-wavelength spin carriers demonstrated here opens up new prospects for THz antiferromagnetic magnonics and coherence-mediated logic devices at THz frequencies.**

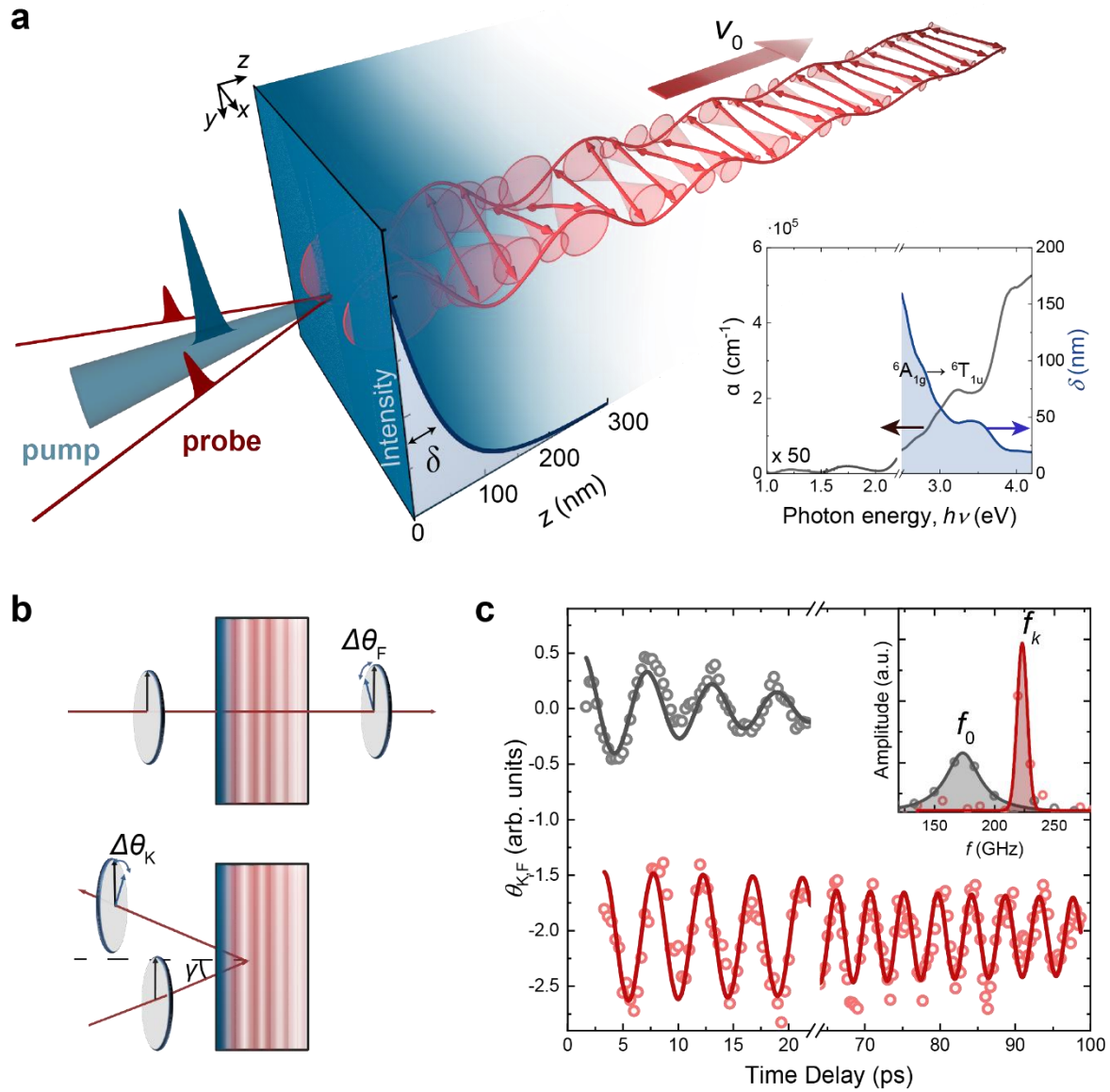
Antiferromagnetic insulators (AFMs) are prime candidates to replace ferromagnets (FMs) as active media in the quest towards high-speed spin transport and large spectral bandwidth operation<sup>6-8</sup>. Integration of AFMs in future wave-based technologies<sup>3</sup> crucially requires the realization of coherent (ballistic) transport of antiferromagnetic spin waves over large distances<sup>5</sup>. In this regard, non-uniform spin-wave modes with short wavelengths ( $\lambda \lesssim 100$  nm) are of particular importance: they can operate at THz clock rates, exhibit high propagation velocities and enable the miniaturization of devices down to the nanoscale. Phase-coherent ballistic spin transport in AFMs

40 is also interesting from a fundamental point of view, as it is predicted to be a prerequisite for the  
41 occurrence of exotic phenomena such as magnetic solitons<sup>12</sup>, Bose-Einstein condensates<sup>13,14</sup> and  
42 spin-superfluidity<sup>15-17</sup>. These prospects call for efficient methods for the excitation, manipulation,  
43 and detection of short-wavelength coherent antiferromagnetic magnons.

44  
45 Conventional methods of linear spin-wave excitation use spatially varying oscillating magnetic  
46 fields. However, the high-frequency THz resonances inherent to antiferromagnetic dynamics make  
47 traditional field sources based on microstrip lines or coplanar waveguides impractical to be used  
48 in antiferromagnetic media. As a result, recent demonstrations of magnon-mediated spin transport  
49 in antiferromagnets were represented either by diffusive propagation of incoherent magnons<sup>9-11</sup> or  
50 by evanescent spin-wave modes<sup>18</sup>, and the generation of coherent propagating short-wavelength  
51 magnons leading to phase-coherent transport in an antiferromagnet has yet to be experimentally  
52 realized.

53  
54 Ultrashort pulses of light have been routinely used to generate and to control large-amplitude THz  
55 spin precession<sup>19-21</sup> in antiferromagnets. The small photon momentum, however, poses a problem:  
56 it gives rise to a large momentum mismatch with short-wavelength spin waves. Consequently,  
57 optical techniques have so far been restricted to the generation of  $k = 0$  uniform antiferromagnetic  
58 magnons and/or pairs of mutually coherent magnons at the edges of the Brillouin zone<sup>22</sup>, for which  
59 group velocities are (near-)zero and no spatial transport of energy and angular momentum takes  
60 place. Here we overcome this problem and present an all-optical method to excite and detect a  
61 broadband wavepacket of short-wavelength coherent propagating magnons in an insulating  
62 antiferromagnet. Optical excitation of intense charge-transfer electronic transitions using  
63 ultrashort pulses in the prototypical antiferromagnet DyFeO<sub>3</sub> provides strong confinement of the  
64 optical field, which creates a narrow exponential profile of deflected spins near the sample surface.  
65 This magnetic non-uniformity extends over the nanoscale penetration depth of the light and serves  
66 as a source of short-wavelength coherent spin waves propagating into the sample bulk, as  
67 illustrated in Figure 1a. Using  $k$ -selective magneto-optical Bragg detection we map out spectral  
68 components of the magnon wavepacket and reveal magnon modes with nanoscale wavelengths,  
69 supersonic group velocities and an estimated propagation length of more than 1  $\mu\text{m}$ .

70



72

73 **Figure 1: All-optical generation and detection of coherent antiferromagnetic spin waves.** (a) Schematic  
 74 illustration of the generation and detection of propagating antiferromagnetic spin waves after excitation of strongly  
 75 absorbing electronic transitions. The optical penetration depth  $\delta$  of the light defines the excited region and the width  
 76 of the magnetic non-uniformity. Inset: Absorption coefficient (left axis) and corresponding penetration depth (right  
 77 axis) for  $\text{DyFeO}_3$  as function of photon energy (see methods).  ${}^6A_{1g} \rightarrow {}^6T_{1u}$ : the charge-transfer transition of interest.  
 78 (b) Schematics for the optical detection mechanisms of spin waves in transmission (top) and reflection (bottom)  
 79 geometries, measuring transient changes in the Faraday rotation ( $\theta_F$ ) and Kerr rotation ( $\theta_K$ ) respectively;  $\gamma$  is the angle  
 80 of incidence. (c) Time-resolved measurements of the polarization rotation of a near-infrared probe pulse after  
 81 excitation with pump pulses with a photon energy of 3.1 eV in the detection geometries shown in (b). The thick solid

82 lines are exponentially damped sine fits. Inset: Fourier spectra of the oscillations with Lorentzian fits (thick solid  
83 lines), with central frequencies  $f_0$  (transmission geometry) and  $f_k$  (reflection geometry). a.u.: arbitrary units.

84

85 Dysprosium orthoferrite ( $\text{DyFeO}_3$ ) is a charge-transfer antiferromagnetic insulator with the Néel  
86 temperature  $T_N = 645$  K, exhibiting one of the strongest observed interactions between spins and  
87 laser pulses<sup>19,23,24</sup>. The optical spectrum of  $\text{DyFeO}_3$  is dominated by a set of intense electronic O-  
88 Fe ( $2p$ - $3d$ ) charge-transfer (CT) transitions. The absorption due to these transitions sets in above  
89 2 eV, and promptly brings the absorption coefficient to values as high as  $5 \times 10^5 \text{ cm}^{-1}$  (see inset Fig.  
90 1a)<sup>25</sup>. Such strong absorption enables confinement of light down to penetration depths ( $\delta$ ) of less  
91 than 50 nm.

92

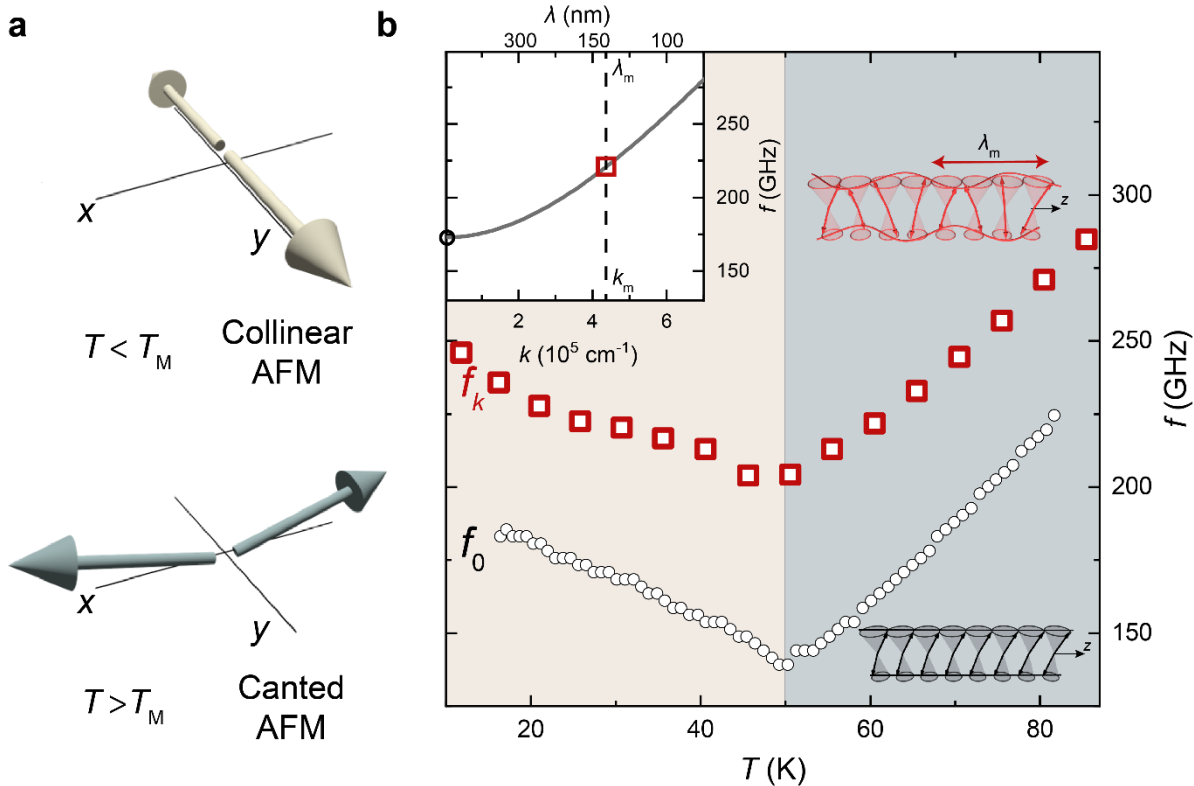
93 In our experiments we study a 60  $\mu\text{m}$  thick slab of  $z$ -cut  $\text{DyFeO}_3$ . The sample is excited with 100 fs  
94 pump pulses which have photon energy tunable in the spectral range of 1.5 - 3.1 eV, covering the  
95 lowest energy  ${}^6\text{A}_{1g} \rightarrow {}^6\text{T}_{1u}$  charge-transfer electronic transition<sup>25</sup>. We use time-delayed probe pulses  
96 at various photon energies below the fundamental absorption gap ( $h\nu < 2$  eV) to detect the photo-  
97 induced magnetic dynamics, see Extended Data Fig. 1. The probing is simultaneously performed  
98 in two complementary experimental geometries: a transmission geometry using the Faraday effect  
99 and a reflection geometry, using the magneto-optical Kerr effect (MOKE) (see Fig. 1b). In both  
100 geometries, the pump-induced rotation of the probe polarization plane, originating from the  
101 Faraday effect ( $\theta_F$ ) or the MOKE ( $\theta_K$ ), is tracked as a function of the pump-probe time delay. Note  
102 that while the Faraday transmission geometry is routinely used in pump-probe experiments for  
103 detecting uniform ( $k = 0$ ) spin precession in antiferromagnets<sup>19</sup>, the reflection geometry has been  
104 shown to enable detection of finite- $k$  coherent excitations such as propagating acoustic  
105 wavefronts<sup>26,27</sup>. As shown below we demonstrate that the reflection geometry can be also used to  
106 probe the dynamics of short-wavelength propagating coherent spin waves.

107

108 Following the optical pumping in the regime of strong absorption ( $h\nu = 3.1$  eV,  $\delta = 50$  nm) the  
109 time-resolved dynamics of the probe polarization reveal high-frequency oscillations in the  
110 hundreds of GHz range (see Fig. 1c). The frequencies  $f_0$  and  $f_k$  of the oscillations observed in the  
111 transmission and reflection geometry respectively, are substantially different:  $f_k > f_0$  (see inset Fig.  
112 1c). Notably, the decay time of the oscillations also differ by nearly an order of magnitude.

113

114 To identify the origin of the oscillations, we track their central frequency as a function of  
 115 temperature. The antiferromagnetic state in DyFeO<sub>3</sub> adopts two distinct spin arrangements, sharply  
 116 separated by a first-order phase transition at the so-called Morin temperature  $T_M \approx 50$  K<sup>28</sup>. At  
 117  $T < T_M$ , the antiparallel iron spins are oriented along the  $y$ -axis and arranged in a compensated  
 118 collinear AFM pattern. Above  $T_M$ , the spins experience a reorientation towards the  $x$ -axis  
 119 accompanied by the mutual canting and stabilization of a canted AFM phase (see Fig. 2a). The  
 120 experimentally acquired temperature dependence of the oscillation frequency exhibits a  
 121 characteristic cusp-like softening with a minimum at  $T_M$  (see Fig. 2b and Extended Data Fig. 2).  
 122 This frequency softening is an unambiguous hallmark of the so-called quasi-antiferromagnetic ( $q$ -  
 123 AFM) magnon branch in DyFeO<sub>3</sub> and is caused by strong temperature variations of the magneto-  
 124 crystalline anisotropy in the vicinity of the spin-reorientation phase transition<sup>29</sup>. Indeed, the  
 125 frequencies  $f_0$  of the oscillations observed in the transmission geometry perfectly match values  
 126 reported in literature for the zone-centre ( $k = 0$ )  $q$ -AFM magnon<sup>29</sup>.



127  
 128 **Figure 2: Generation and detection of coherent finite- $k$  antiferromagnetic spin waves.** (a) The spin orientation in  
 129 the collinear AFM (top panel) and canted AFM phase (bottom panel). (b) Temperature ( $T$ ) dependence of the central  
 130 frequency of the oscillatory dynamics as measured in the reflection geometry (red square markers) after excitation  
 131 with strongly absorbed pump pulses ( $h\nu = 3.1$  eV,  $\delta = 50$  nm) compared with the  $k = 0$  magnon  $T$ -dependence, as

132 measured in standard transmission geometry (black circle markers). See also Extended Data Fig. 2. Left top inset: The  
 133 antiferromagnetic magnon dispersion of DyFeO<sub>3</sub> and the wavenumbers of the magnons observed in the reflection and  
 134 transmission experimental geometries. Right insets: Schematic illustration of the spin wave corresponding to the  
 135 oscillatory dynamics at the different frequencies.

136

137 To explain the physical origin of the oscillation at frequency  $f_k$  seen in the MOKE experiment, we  
 138 refer to the dispersion relation for magnon modes in antiferromagnets. In both magnetic phases,  
 139 below and above  $T_M$ , the magnon spectrum  $\omega_k$  in DyFeO<sub>3</sub>, is given by<sup>30</sup>:

$$140 \quad \omega_k = \sqrt{\omega_0^2 + (v_0 k)^2}, \quad (1)$$

141 where  $v_0 \approx 20$  km/s is the limiting group velocity of the spin waves<sup>30</sup>. This dispersion relation is  
 142 schematically shown as an inset to Fig. 2b. At small wavenumbers  $kv_0 \ll \omega_0$ , it has a quadratic  
 143 form due to the magnon gap  $\omega_0 = 2\pi f_0$ , arising from magneto-crystalline anisotropy. At larger  
 144 wavenumbers ( $v_0 k \gg \omega_0$ ), the dispersion relation becomes dominated by the exchange interaction  
 145 (exchange regime), and thus takes a linear form typical for antiferromagnets<sup>30</sup>. We identify the  
 146 MOKE signal at  $f_k$  as a finite- $k$  magnon on the  $q$ -AFM branch: it follows the characteristic  
 147 temperature dependence of the  $f_0$  zone-center magnon mode and has a nearly temperature-  
 148 independent blueshift. The detection geometry implies that the magnon wavevector  $\mathbf{k}$  is  
 149 perpendicular to the sample surface, and its magnitude can be deduced from Eq. (1) to be  
 150  $k = 4.2 \times 10^5 \text{ cm}^{-1}$  ( $\lambda \approx 140$  nm), as marked on the inset to Figure 2b.

151

152 By considering the modulation of the material's dielectric tensor due to the propagating coherent  
 153 spin waves, the attribution of the  $f_k$  oscillation to a finite- $k$  magnon on the  $q$ -AFM branch can be  
 154 further supported. A spin wave with a propagation vector along the  $z$ -axis results in a perturbation  
 155 of the magnetic order and a corresponding periodic modulation of the off-diagonal components of  
 156 the dielectric tensor<sup>31</sup>. In this way the spin waves in the medium produce the magneto-optical  
 157 analogue of a dynamical volume phase grating for the probe light wave. The polarization state of  
 158 the reflected probe is explained by the Bragg reflection of light from this diffraction grating, an  
 159 approach similar to the one used in Brillouin light scattering studies on spin waves<sup>32</sup>. As a result,  
 160 the polarization rotation of the reflected probe beam with wavenumber  $k_0$  becomes subject to a  
 161 Bragg condition:

$$162 \quad k_m = 2k_0 n(\lambda_0) \cos \gamma', \quad (2)$$

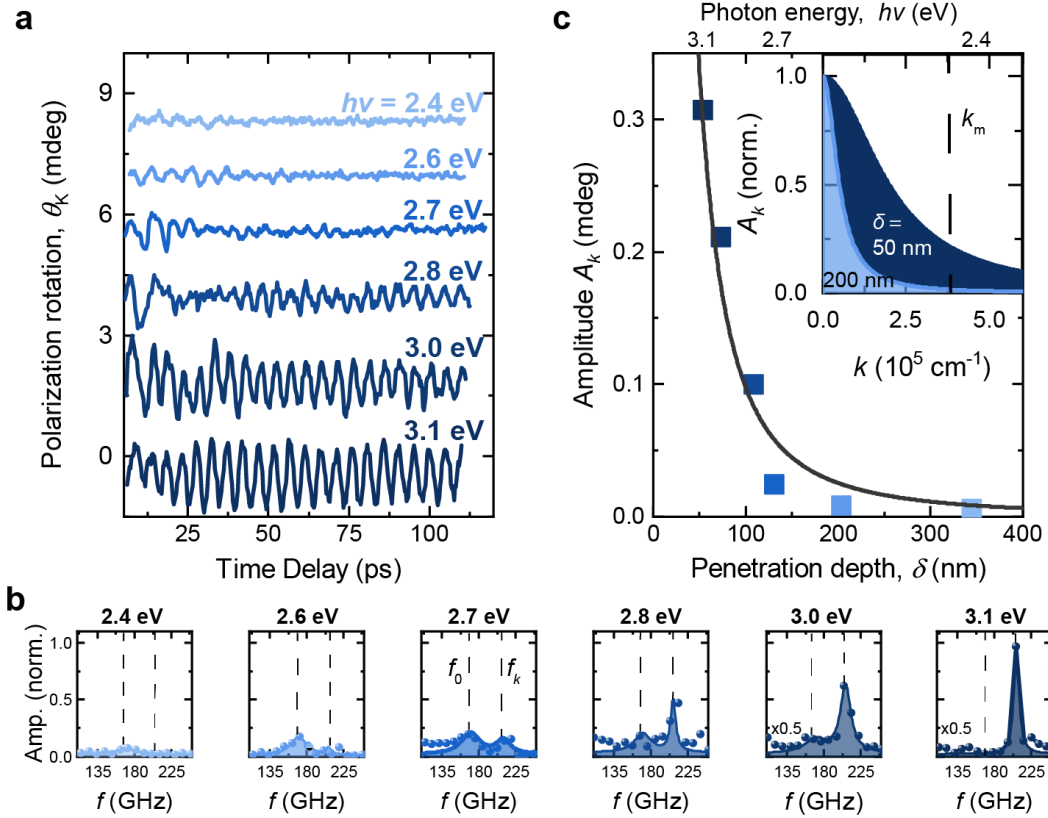
163 where  $n(\lambda_0)$  is the optical refractive index of the medium at the probe wavelength  $\lambda_0$ ,  $\gamma'$  is the  
164 refracted angle of incidence of the probe, and  $k_m$  is the normal projection of the  $\mathbf{k}$ -vector of the  
165 magnon to which the probe pulse is sensitive (see Supplementary section S1). Using Eq. (2) we  
166 find that a probe pulse at a central wavelength of 680 nm ( $n \approx 2.39$ )<sup>25</sup> and normal incidence ( $\gamma' = 0$ )  
167 is sensitive to propagating magnons with wavenumber  $k \approx 4.2 \times 10^5 \text{ cm}^{-1}$ . Note that this independent  
168 estimation perfectly matches the magnon wavenumber retrieved using the measured frequency and  
169 known dispersion relation (Eq. (1)).

170

171 The generation and detection of finite- $k$  coherent magnons is anticipated to rely strongly on the  
172 confinement provided by the optical penetration depth  $\delta$ , which is highly dispersive near the  
173 charge-transfer band. In particular, changing the pump photon energy between 2.4 eV and 3.1 eV  
174 provides a variation in the penetration depth between 300 and 50 nm, while the real part of the  
175 refractive index (influencing the pump wavelength) changes by only 5% (see Extended Data Fig.  
176 3). Therefore, we expect that by changing the photon energy of the pump pulses, the amplitude of  
177 the finite- $k$  magnon will vary strongly. The time-resolved MOKE signals obtained in the reflection  
178 geometry for different photon energies of the pump excitation, are shown in Fig. 3a. The Fourier  
179 transforms of the signals (Fig. 3b) show that the spectra are composed of two components,  
180 corresponding to the zone-centre and finite- $k$  ( $k = 3.7 \cdot 10^5 \text{ cm}^{-1}$ ) magnon modes. We observe that  
181 with increasing photon energy (i.e. decreasing penetration depth), the amplitude of the finite- $k$   
182 magnon mode increases dramatically. The magnon amplitude extracted for the pump excitation at  
183 different photon energies, as a function of the corresponding penetration length, is shown in Fig.  
184 3c. The obtained dependence shows that the finite- $k$  magnon is nearly absent for penetration depths  
185 larger than 150 nm, a value close to the wavelength of the detected magnons, and grows  
186 dramatically for shorter penetration lengths.

187

188



190

191

192

193

194

195

196

197

198

199

200

201

202

203

204

205

206

207

**Figure 3: Confinement of the light as a necessary condition for the generation of high- $k$  spin waves.** (a) Time-resolved signals of the polarization rotation of the near-infrared probe pulse after excitation with pump pulses with increasing photon energy in a reflection geometry. (b) Fourier amplitude spectra of the time-resolved signals from panel (a). (c) Amplitude of sine fit oscillations corresponding to the AFM propagating spin wave to the data from panel (a) vs penetration depth of the excitation pulse (color markers correspond to traces in panel (a)). The solid line is a fit using  $I_0/(1 + (k\delta)^2)$ . Inset: Magnon frequency distribution after excitation with pump pulses with  $\delta = 50 \text{ nm}$  (dark blue, broadband distribution) and  $200 \text{ nm}$  (light blue, narrowband). The probe is sensitive to  $k_m = 3.7 \cdot 10^5 \text{ cm}^{-1}$ , indicated by the dashed line.

We model this observation using a simple assumption: the ultrashort light pulse promotes a spin excitation that is strongly non-uniform along the direction of incidence  $z$ . The excitation leads to a nearly instantaneous deflection of spins by an angle  $\varphi(z)$  with the spatial distribution following the optical absorption profile given by the Beer-Lambert law:  $\varphi(z, t=0) = \varphi_0 e^{-z/\delta}$ , where  $\varphi_0 \sim I_0/\delta$  is proportional to the intensity of the pump pulse  $I_0$ , and inversely proportional to the light penetration depth  $\delta$  (see Supplementary section S2). The strongly non-uniform spin excitation distributes the initial deflection among magnon modes at different  $k$ -wavenumbers, with the amplitudes given by the reciprocal space image  $A_k$  of the initial excitation set up by the penetration

208 depth (see inset Fig. 3c). As a result, the finite- $k$  mode is expected to have spectral amplitude  $A_k$   
 209 (see Supplementary Section S2):

$$210 \quad A_k \sim \frac{I_0}{1+(k\delta)^2} \quad (3)$$

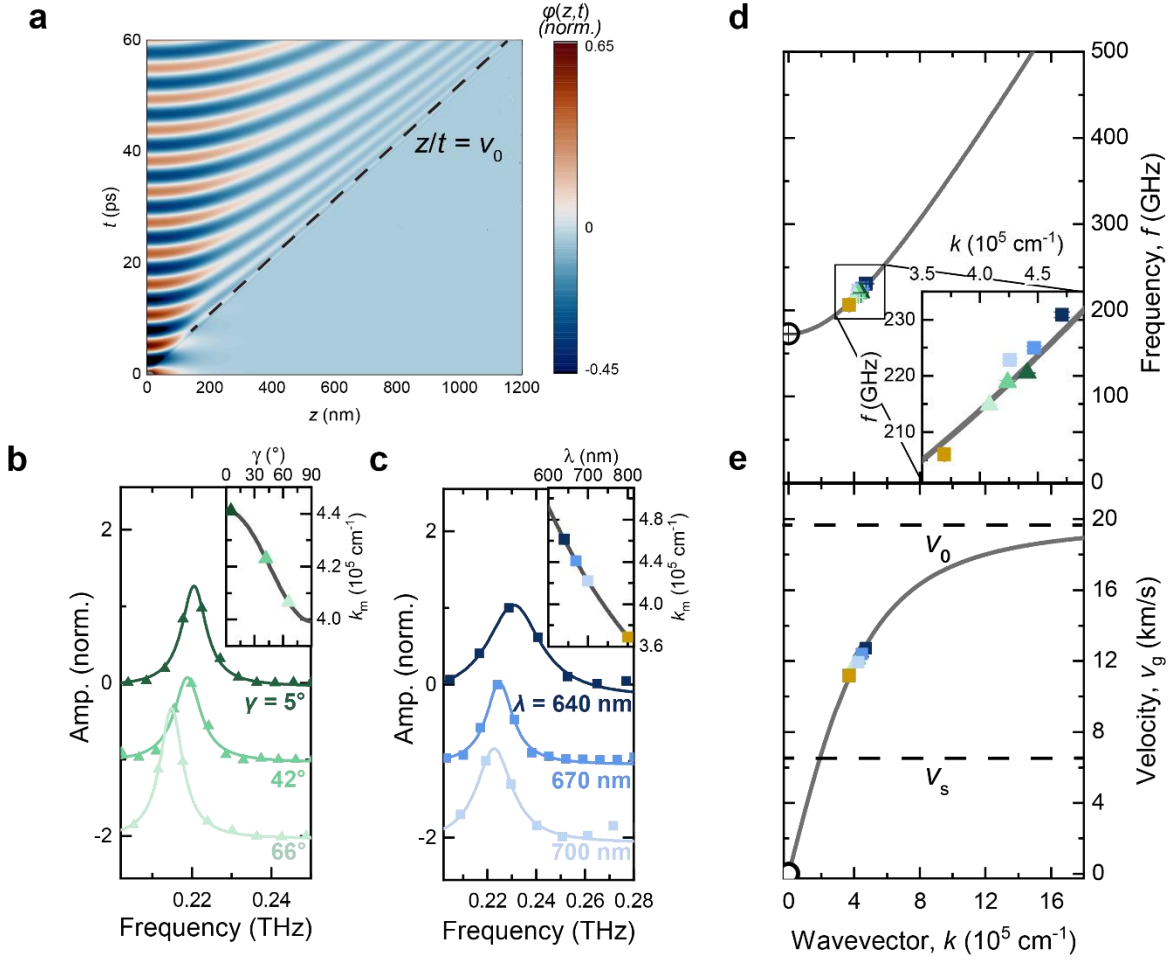
211 This expression not only agrees well with the observations of Fig. 3c ( $k \approx 3.7 \times 10^5 \text{ cm}^{-1}$ ,  
 212  $\lambda = 170 \text{ nm}$ ), where it is plotted as a best fit to the pump intensity  $I_0$ , but also confirms the intuitive  
 213 interpretation that a stronger confinement shifts the spectral amplitude of the excited magnon wave  
 214 packet towards larger  $k$ .

215  
 216 The excitation of a continuum of coherent antiferromagnetic spin waves forms a broadband  
 217 magnon wavepacket, in which individual spectral components propagate independently, each  
 218 adhering to the dispersion relation  $\omega_k = 2\pi f_k$  (Eq. (1)). In order to visualize the time evolution of  
 219 the excited magnon wavepacket, we make use of the linearized sine-Gordon equation for the space-  
 220 ( $z$ ) and time- ( $t$ ) dependent amplitude of the spin deflections  $\varphi(z,t)^{30}$ . We find that the evolution of  
 221 the spin dynamics is described by the following simple formula (see Supplementary section S2):

$$222 \quad \varphi(z, t) = \frac{2}{\pi} \int_{-\infty}^{\infty} dk [A_k \cos(kz) \cos(\omega_k t)] \quad (4)$$

223 By integrating this equation, under the assumption of the exponential distribution of the time-zero  
 224 spin deflections and  $\delta = 50 \text{ nm}$ , we obtain the complete dynamics of the magnetic excitation. As  
 225 shown in Fig. 4a and Extended Data Fig. 4, the strong dispersion promptly smears out the initial  
 226 exponential profile of the spin excitation simultaneously forming a spin-wave front after  $\sim 10 \text{ ps}$   
 227 that propagates into the bulk. This front is composed by the short-wavelength magnons with  
 228  $k \gtrsim 20 \times 10^5 \text{ cm}^{-1}$  propagating with the limiting group velocity  $v_0$ .

229  
 230 Applying the Bragg condition of Eq. (2), we can experimentally map out the spectral components  
 231 of the excited broadband magnon wave packet, as well as determine the group velocity and  
 232 propagation length of individual magnon modes. First, we vary the incidence angle  $\gamma$  of the probe  
 233 pulse, (inset Fig. 4b) and find that the central frequency of the oscillations is



234

235

**Figure 4: Revealing spectral components of the broadband antiferromagnetic magnon wavepacket.** (a)

236

Simulation of the time- and position-dependent spin deflection  $\phi(z,t)$  after optical excitation at 3.1 eV with a

237

penetration depth of 50 nm, as determined by Eq. (3). (b,c) Fourier spectra of time-resolved measurements of the

238

polarization rotation of a near-infrared probe pulse obtained in the reflection geometry after excitation with pump

239

pulses with a photon energy of 3.1 eV at the temperature  $T = 60$  K for different probe incidence angles  $\gamma$  ( $\lambda = 680$  nm)

240

(a) and probe wavelengths  $\lambda$  ( $\gamma = 5^\circ$ ) (b). The solid superimposed lines are Lorentzian fits of the Fourier peaks. Insets:

241

The magnon wavenumber  $k_m$  to which the probe is sensitive, as a function of the angle  $\gamma$  (b) and probe wavelength  $\lambda$

242

(c), with the measured points indicated by coloured markers. (d,e) The extracted central magnon frequencies (d) and

243

the calculated group velocity (e) from the data in panel (b) and (c) at their respective calculated wavenumbers plotted

244

with a best fit of the spin-wave dispersion curve (d) and the group velocity corresponding to the dispersion fit (e). The

245

marker colours and shapes correspond to the measurements in panel (b) and (c).

246

247

reduced upon increasing  $\gamma'$  (Fig. 4b), in perfect agreement with Eq. (2) and the magnon dispersion

248

of Eq. (1). Next, upon decreasing the probe wavelength, we observe a systematic increase in the

249

magnon frequency, as shown in Fig. 4c, once again in accordance with the Bragg condition. To

250 summarize our observations, we plot the extracted central frequencies as a function of the  
 251 corresponding wavenumbers  $k_m$  (see Fig. 4d). These points are fit to the dispersion relation given  
 252 by Eq. (1), with the spin-wave gap  $\omega_0$  defined by the experimentally obtained zone-center magnon  
 253 frequency. The best fit of the experimental data yields a limiting group  
 254 velocity  $v_0 = 19.7 \pm 0.1$  km/s. This value stands in good agreement with the limiting group  
 255 velocity of  $\sim 20$  km/s extracted from the speed limit of the magnetic domain walls in DyFeO<sub>3</sub>, as  
 256 reported in Ref. [30]. Using the extracted value of the limiting group velocity we evaluate the  
 257 group velocities  $v_g = \left. \frac{\partial \omega_k}{\partial k} \right|_{k=k_m}$  of the optically detected magnons given by  $v_g = v_0^2 \frac{k_m}{\omega_k}$ . These  
 258 values, shown in Fig. 4e, indicate that while the zone-center magnons do not support propagation,  
 259 the shortest-wavelength components of the magnon wavepacket detected in our experiment  
 260 ( $\lambda = 125$  nm) propagate at a supersonic ( $v_s = 6$  km/s, see Supplementary Section S3) velocity of  
 261 nearly 13 km/s. We note that magnons with these wavelengths already approach the exchange  
 262 wave regime characterized by the limiting group velocity  $v_0$ . This remarkable feature, inherent to  
 263 antiferromagnets, stands in sharp contrast with the situation in ferromagnets, where the quadratic  
 264 dispersion relation dictates that the exchange value of the group velocity is reached only for  
 265 magnons with  $\lambda_m \lesssim 10$  nm. Although the shortest magnon wavelength detected in our experiments  
 266 is 125 nm, magnons at even shorter wavelengths, down to the penetration depth limit of 50 nm,  
 267 are anticipated, and could be detected using probe pulses at higher photon energies or other means  
 268 to measure non-local ultrafast spin excitations<sup>33-35</sup>. Using the extracted lifetime of the oscillations  
 269  $\tau = 85$  ps (see Extended Data Fig. 5), we estimate the coherence length  $l_c$  of the spin-wave transport  
 270  $l_c = v_g \tau = 1.1$   $\mu\text{m}$ . We note that this length, dramatically enhanced as compared to metallic  
 271 antiferromagnets<sup>8,36</sup>, also agrees with studies of diffusive spin transport in other insulating  
 272 antiferromagnets<sup>9,37</sup>. One can anticipate even longer propagation lengths for the coherent (ballistic)  
 273 regime reported here: our estimate of the coherence length is only a lower limit, as the propagating  
 274 spin wave is likely to escape from the region that is probed by the reflected probe light ( $\sim \lambda/2$ ).  
 275 These striking observations make antiferromagnetic insulators such as DyFeO<sub>3</sub> a promising  
 276 platform for the realization of high-speed wave-based magnonic devices.

277

278 By optical pumping of above-bandgap electronic transitions, we have explored an efficient and  
 279 virtually universal route to launch coherent propagating spin waves in insulating antiferromagnets.  
 280 The strong optical absorption provides an opportunity to spatially confine the light to a

281 subwavelength scale, inaccessible by any other means, e.g. focusing<sup>38-40</sup>, enabling the emission of  
282 a broadband continuum of short-wavelength antiferromagnetic magnons. The universal  
283 mechanism opens up prospects for terahertz coherent AFM magnonics and opto-spintronics<sup>7</sup>  
284 providing a long-sought source of coherent high-velocity spin waves. We anticipate even higher  
285 propagation velocities to be observed in the broad class of easy-plane antiferromagnets (e.g.  
286 hematite<sup>37</sup> and FeBO<sub>3</sub>), in which the spin-wave gap  $\omega_0$  is reduced and the high-velocity exchange  
287 wave regime can be achieved at significantly smaller wavenumbers  $k$ . The demonstrated approach  
288 holds promise for a wide range of fundamental studies exploiting the excitation and propagation  
289 of non-linear spin waves such as magnetic solitons<sup>12,41</sup> as well as the investigation of the giant  
290 magneto-elastic coupling between antiferromagnetic magnons and acoustic phonons<sup>42</sup> directly in  
291 the time-domain.

292

## 293 **References**

294

- 295 1 Kruglyak, V. V. & Hicken, R. J. Magnonics: Experiment to prove the concept. *J. Magn.*  
296 *Magn. Mater.* **306**, 191-194 (2006).
- 297 2 Kruglyak, V. V., Demokritov, S. & Grundler, D. Magnonics. *J. Phys. D* **43**, 264001 (2010).
- 298 3 Lenk, B., Ulrichs, H., Garbs, F. & Münzenberg, M. The building blocks of magnonics.  
299 *Phys. Rep.* **507**, 107-136 (2011).
- 300 4 Chumak, A. V., Vasyuchka, V. I., Serga, A. A. & Hillebrands, B. Magnon spintronics. *Nat.*  
301 *Phys.* **11**, 453-461 (2015).
- 302 5 Sander, D. *et al.* The 2017 magnetism roadmap. *J. Phys. D* **50**, 363001 (2017).
- 303 6 Jungwirth, T., Marti, X., Wadley, P. & Wunderlich, J. Antiferromagnetic spintronics. *Nat.*  
304 *Nanotechnol.* **11**, 231-241 (2016).
- 305 7 Němec, P., Fiebig, M., Kampfrath, T. & Kimel, A. V. Antiferromagnetic opto-spintronics.  
306 *Nat. Phys.* **14**, 229-241 (2018).
- 307 8 Baltz, V. *et al.* Antiferromagnetic spintronics. *Rev. Mod. Phys.* **90**, 015005 (2018).
- 308 9 Lebrun, R. *et al.* Tunable long-distance spin transport in a crystalline antiferromagnetic  
309 iron oxide. *Nature* **561**, 222-225 (2018).
- 310 10 Li, J. *et al.* Spin current from sub-terahertz-generated antiferromagnetic magnons. *Nature*  
311 **578**, 70-74 (2020).

- 312 11 Vaidya, P. *et al.* Subterahertz spin pumping from an insulating antiferromagnet. *Science*  
313 **368**, 160-165 (2020).
- 314 12 Galkina, E. & Ivanov, B. Dynamic solitons in antiferromagnets. *Low. Temp. Phys.* **44**, 618-  
315 633 (2018).
- 316 13 Giamarchi, T., Rüegg, C. & Tchernyshyov, O. Bose–Einstein condensation in magnetic  
317 insulators. *Nat. Phys.* **4**, 198-204 (2008).
- 318 14 Johansen, Ø., Kamra, A., Ulloa, C., Brataas, A. & Duine, R. A. Magnon-mediated indirect  
319 exciton condensation through antiferromagnetic insulators. *Phys. Rev. Lett.* **123**, 167203  
320 (2019).
- 321 15 Bunkov, Y. M. *et al.* High- $T_c$  spin superfluidity in antiferromagnets. *Phys. Rev. Lett.* **108**,  
322 177002 (2012).
- 323 16 Takei, S., Halperin, B. I., Yacoby, A. & Tserkovnyak, Y. Superfluid spin transport through  
324 antiferromagnetic insulators. *Phys. Rev. B* **90**, 094408 (2014).
- 325 17 Qaiumzadeh, A., Skarsvåg, H., Holmqvist, C. & Brataas, A. Spin superfluidity in biaxial  
326 antiferromagnetic insulators. *Phys. Rev. Lett.* **118**, 137201 (2017).
- 327 18 Dąbrowski, M. *et al.* Coherent transfer of spin angular momentum by evanescent spin  
328 waves within antiferromagnetic NiO. *Phys. Rev. Lett.* **124**, 217201 (2020).
- 329 19 Kimel, A. *et al.* Ultrafast non-thermal control of magnetization by instantaneous  
330 photomagnetic pulses. *Nature* **435**, 655-657 (2005).
- 331 20 Duong, N., Satoh, T. & Fiebig, M. Ultrafast manipulation of antiferromagnetism of NiO.  
332 *Phys. Rev. Lett.* **93**, 117402 (2004).
- 333 21 Kampfrath, T. *et al.* Coherent terahertz control of antiferromagnetic spin waves. *Nat.*  
334 *Photonics* **5**, 31-34 (2011).
- 335 22 Bossini, D. *et al.* Macrospin dynamics in antiferromagnets triggered by sub-20  
336 femtosecond injection of nanomagnons. *Nat. Commun.* **7**, 1-8 (2016).
- 337 23 Afanasiev, D. *et al.* Ultrafast control of magnetic interactions via light-driven phonons.  
338 *Nat. Mater.*, 1-5 (2021).
- 339 24 Afanasiev, D. *et al.* Control of the ultrafast photoinduced magnetization across the Morin  
340 transition in DyFeO<sub>3</sub>. *Phys. Rev. Lett.* **116**, 097401 (2016).
- 341 25 Usachev, P. *et al.* Optical properties of thulium orthoferrite TmFeO<sub>3</sub>. *Phys. Solid State* **47**,  
342 2292-2298 (2005).

343 26 Thomsen, C., Grahn, H. T., Maris, H. J. & Tauc, J. Surface generation and detection of  
344 phonons by picosecond light pulses. *Phys. Rev. B* **34**, 4129 (1986).

345 27 Hortensius, J. R., Afanasiev, D., Sasani, A., Bousquet, E. & Caviglia, A. D. Ultrafast strain  
346 engineering and coherent structural dynamics from resonantly driven optical phonons in  
347  $\text{LaAlO}_3$ . *npj Quantum Mater.* **5**, 1-6 (2020).

348 28 Afanasiev, D., Zvezdin, A. & Kimel, A. Laser-induced shift of the Morin point in  
349 antiferromagnetic  $\text{DyFeO}_3$ . *Opt. Express* **23**, 23978-23984 (2015).

350 29 Balbashov, A., Volkov, A., Lebedev, S., Mukhin, A. & Prokhorov, A. High-frequency  
351 magnetic properties of dysprosium orthoferrite. *Zh. Eksp. Teor. Fiz. [Sov. Phys. JETP]* **88**,  
352 974-987 (1985).

353 30 Bar'yakhtar, V. G., Ivanov, B. & Chetkin, M. V. Dynamics of domain walls in weak  
354 ferromagnets. *Sov. Phys. Usp.* **28**, 563-588 (1985).

355 31 Zvezdin, A. K. & Kotov, V. A. *Modern magneto-optics and magneto-optical materials*.  
356 (CRC Press, 1997).

357 32 Demokritov, S. O., Hillebrands, B. & Slavin, A. N. Brillouin light scattering studies of  
358 confined spin waves: linear and nonlinear confinement. *Phys. Rep.* **348**, 441-489 (2001).

359 33 Qiu, H. *et al.* Ultrafast spin current generated from an antiferromagnet. *Nat. Phys.*, 1-7  
360 (2020).

361 34 Rzdolski, I. *et al.* Nanoscale interface confinement of ultrafast spin transfer torque driving  
362 non-uniform spin dynamics. *Nat. Commun.* **8**, 1-5 (2017).

363 35 Melnikov, A. *et al.* Ultrafast transport of laser-excited spin-polarized carriers in  
364  $\text{Au/Fe/MgO}$  (001). *Phys. Rev. Lett.* **107**, 076601 (2011).

365 36 Siddiqui, S. A. *et al.* Metallic antiferromagnets. *J. Appl. Phys.* **128**, 040904 (2020).

366 37 Lebrun, R. *et al.* Long-distance spin-transport across the Morin phase transition up to room  
367 temperature in the ultra-low damping single crystals of the antiferromagnet  $\alpha\text{-Fe}_2\text{O}_3$  *Nat.*  
368 *Commun.* **11**, 6332 (2020).

369 38 Hashimoto, Y. *et al.* All-optical observation and reconstruction of spin wave dispersion.  
370 *Nat. Commun.* **8**, 1-6 (2017).

371 39 Satoh, T. *et al.* Directional control of spin-wave emission by spatially shaped light. *Nat.*  
372 *Photonics* **6**, 662-666 (2012).

- 373 40 Au, Y. *et al.* Direct excitation of propagating spin waves by focused ultrashort optical  
374 pulses. *Phys. Rev. Lett.* **110**, 097201 (2013).
- 375 41 Bonetti, S. *et al.* Direct observation and imaging of a spin-wave soliton with  $p$ -like  
376 symmetry. *Nat. Commun.* **6**, 1-6 (2015).
- 377 42 Ozhogin, V. & Preobrazhenskiĭ, V. Anharmonicity of mixed modes and giant acoustic  
378 nonlinearity of antiferromagnetics. *Sov. Phys. Usp.* **31**, 713-729 (1988).

379 **Methods**

380

381 **Sample.**

382 A single crystal of DyFeO<sub>3</sub>, 60 μm thick, grown by a floating zone melting technique was used  
383 in this work. The sample is cut perpendicularly to the crystallographic z-axis.

384

385 **Time-resolved experiment.**

386 The experimental setup is schematically shown in Extended Data Figure 1.

387 An amplified 1 kHz Ti:Sapphire laser system (Astrella, Coherent, central wavelength 800 nm,  
388 pulse energy: 7 mJ, pulse duration: 100 fs) forms the basis of the experimental setup. A large  
389 fraction of this output is used to pump a dual optical parametric amplifier (OPA, TOPAS-Twins,  
390 Light Conversion). The OPA delivers linearly polarized, 100 fs output pulses, with photon  
391 energies  $\hbar\omega$  in the range 0.45-1 eV ( $\lambda = 2.7 - 1.4 \mu\text{m}$ ). The photon energy of these output pulses  
392 was doubled or tripled using a  $\beta$ -barium borate (BBO) single crystal in order to obtain tunable  
393 excitation pulses which cover the photon energies in the optical range of 1.5-3.1 eV (wavelength  
394 400-800 nm). A small portion of the amplifier pulses was sent through a mechanical delay line  
395 and used as probe of the spin dynamics in the reflection and transmission geometries.

396 Pump and probe pulse were focused onto the DyFeO<sub>3</sub> sample (pump spot diameter: 300 μm,  
397 typical fluence 2 mJ/cm<sup>2</sup>, probe spot diameter: 80 μm), which was kept in a dry-cycle cryostat  
398 (Montana Instruments) that allowed to cool it down to 10 K and vary the temperature with high  
399 stability in a wide temperature range (10-250 K). The pump-induced changes in the polarization  
400  $\theta_{K,F}$  of the reflected or transmitted probe pulse were measured using an optical polarization  
401 bridge (Wollaston prism) and a pair of balanced Si photodetectors.

402

403 **Experimental determination of the absorption coefficient.**

404 The unpolarised absorption spectrum of DyFeO<sub>3</sub> was directly obtained with light propagating  
405 along the crystal z-axis in the spectral region 1-2.2 eV. The resulting absorption is shown in  
406 Figure 1b. In addition, we performed spectroscopic ellipsometry measurements using a  
407 Woollam M5000 ellipsometer over a wide energy range to obtain the real and imaginary parts  
408 of the refractive index. In the photon energy region 2.5-4 eV, where the transmission  
409 measurements are not possible for thick samples, we estimated the absorption using the  
410 acquired complex refractive index. These values are shown in Figure 1b.

411

412

413

414 **Data Availability:**

415 All data needed to evaluate the conclusions in the paper are present in the paper and/or  
416 Supplementary Materials. The source data for figures are publicly available with identifier  
417 (DOI) 10.5281/zenodo.4716539

418 **Code Availability:**

419 The code used to simulate the magnon dynamics is available upon reasonable request.

420

421 **Acknowledgements:**

422 The authors thank V.V. Kruglyak and R. Rejali for critically reading the manuscript and E.  
423 Demler for useful discussions. This work was supported by the EU through the European  
424 Research Council, Grant No. 677458 (AlterMateria), the Netherlands Organization for  
425 Scientific Research (NWO/OCW) as part of the Frontiers of Nanoscience program (NanoFront)  
426 and the VENI-VIDI-VICI program. R.V.M and R.L. acknowledge support from the European  
427 Research council, Grant No. 852050 (MAGSHAKE). R.C. acknowledges support by the project  
428 Quantox, Grant No. 731473, QuantERA-NET Cofund in Quantum Technologies, implemented  
429 within the EU-H2020 Programme. B.A.I acknowledges support from the National Scientific  
430 Foundation of Ukraine under Grant. No. 2020.02/0261.

431

432 **Author contributions:**

433 D.A. and A.D.C. conceived the project. J.R.H., D.A. and M.M performed the experiments,  
434 analysed the data. B.A.I. developed the general theoretical framework describing the spin wave  
435 propagation. R.L and R.V.M. developed the theoretical formalism of the spin wave detection.  
436 B.A.I., R.C., R.V.M. and A.V.K. contributed to discussion and theoretical interpretation of the  
437 results. A.D.C. supervised the project. The manuscript was written by J.R.H., D.A. and A.D.C.,  
438 with feedback and input from all co-authors.

439

440 **Competing interests:**

441 The authors declare no competing interests.

442

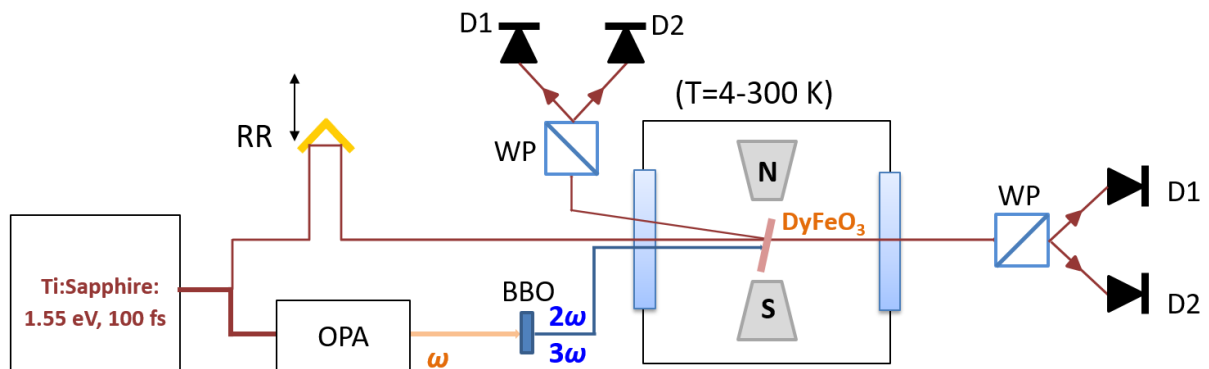
443

444

445 **Extended Data Figures**

446

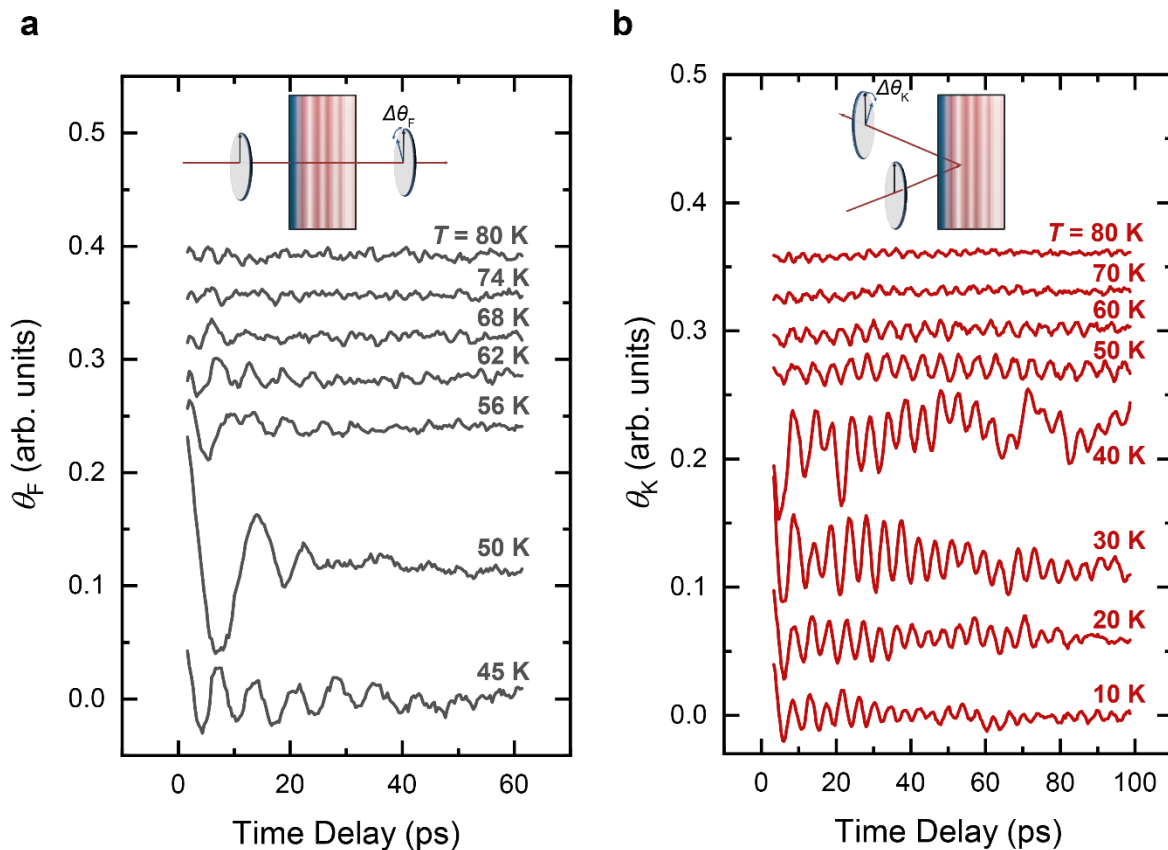
447



448

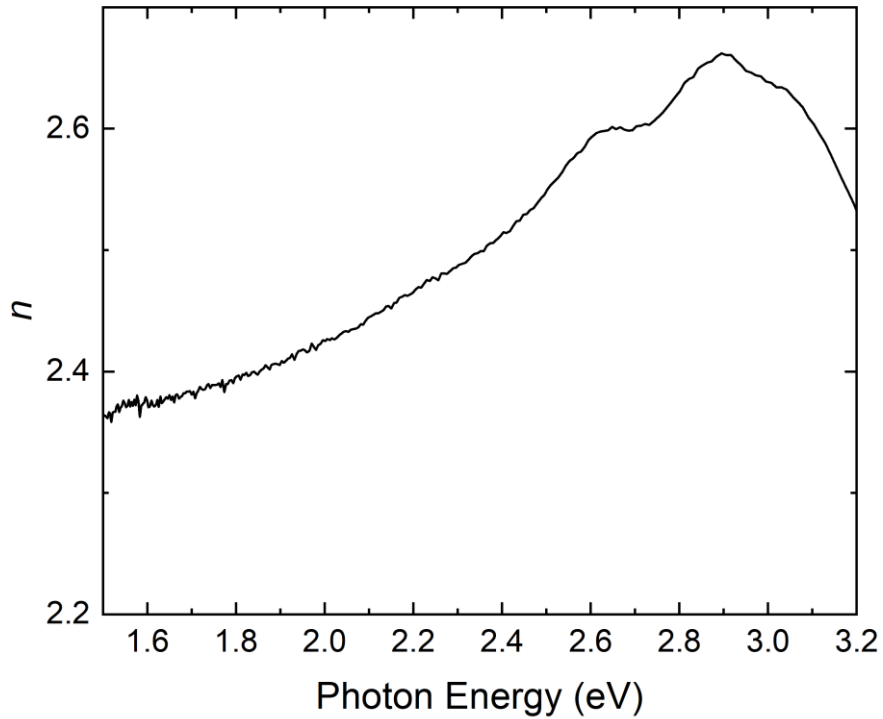
449 **Extended Data Figure 1: Experimental setup.** RR: gold retroreflector mounted on a motorized precision delay  
 450 stage, OPA: optical parametric amplifier, BBO:  $\beta$ -barium borate crystal, WP: Wollaston Prism, D1, D2: pair of  
 451 balanced silicon photodetectors.

452



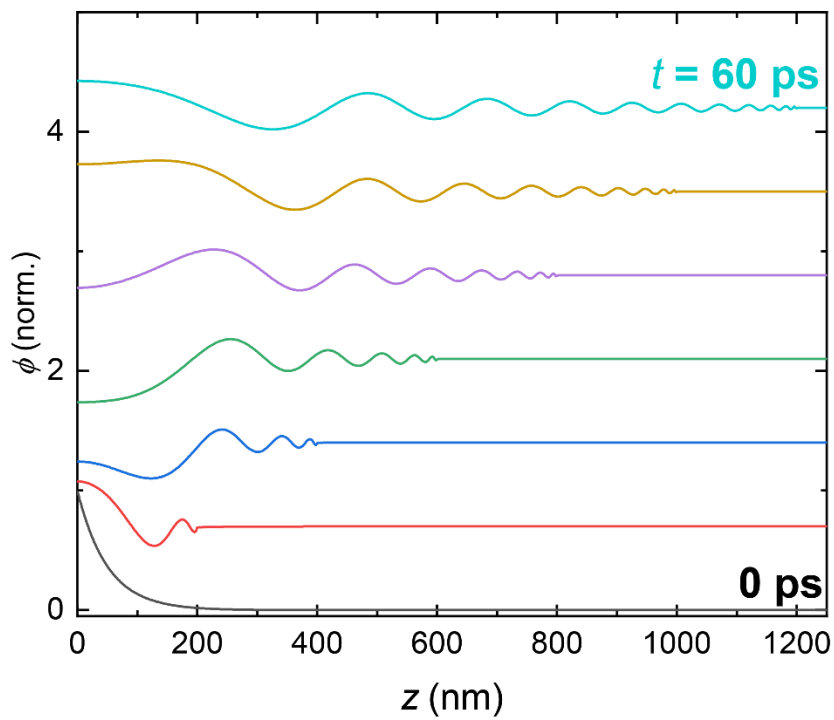
453

454 **Extended Data Figure 2: Magnon time traces at different temperatures.** (a,b) Time resolved polarization  
 455 rotation in the transmission (a) and reflection geometry (b) following excitation at  $h\nu = 3.1$  eV at different  
 456 temperatures. The probe incidence angle is near-normal, with  $\lambda = 640$  nm and  $\lambda = 700$  nm for the measurements  
 457 in panel a and b, respectively.



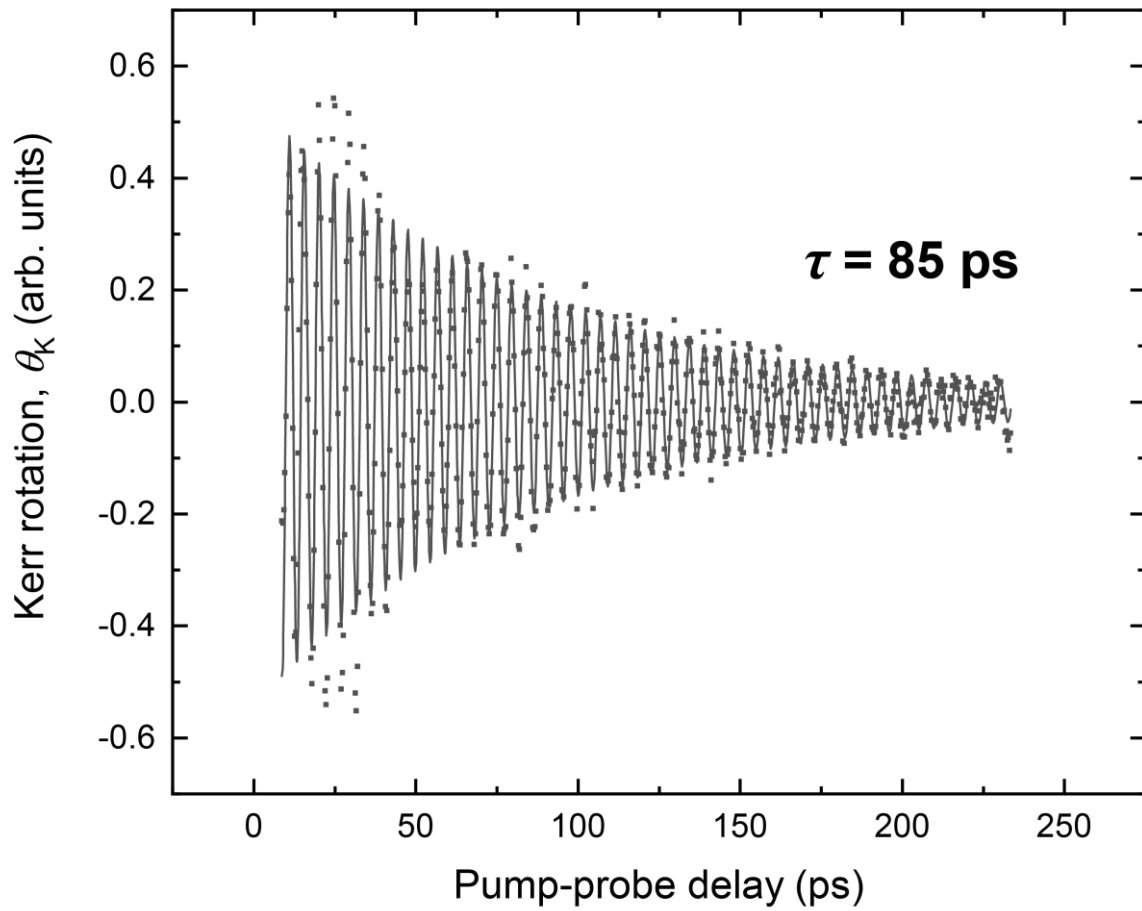
458

459 **Extended Data Figure 3: Real part of the refractive index as a function of the pump photon energy.** Real  
 460 part  $n$  of the refractive index, as extracted using spectroscopic ellipsometry measurements.



461

462 **Extended Data Figure 4: Simulations of the light-induced spin wave dynamics.** Real-space distribution of  
 463 the magnon spin deflection at different times  $t$ , after optical excitation at  $h\nu = 3.1$  eV with a penetration depth of  
 464 50 nm, as determined by Eq. (3).



465

466 **Extended Data Figure 5: Extracting the magnon propagation distance.** Time-resolved polarization rotation  
 467 originating from a propagating magnon, as obtained in the reflection geometry. The solid line represents a best fit  
 468 of a damped sine, giving a lifetime of  $\sim 85$  ps. With the largest estimated group velocities  $v_g$  of the measured  
 469 magnons of about 13 km/s, this gives a propagation distance  $l_c = v_g \tau = 1.1 \mu\text{m}$ .

470